Journal of Applied Physics

Cathodoluminescence spectrum imaging analysis of CdTe thin-film bevels

Cite as: J. Appl. Phys. **120**, 105704 (2016); https://doi.org/10.1063/1.4962286
Submitted: 16 June 2016 . Accepted: 24 August 2016 . Published Online: 09 September 2016

John Moseley, Mowafak M. Al-Jassim, Harvey L. Guthrey, James M. Burst, Joel N. Duenow, Richard K. Ahrenkiel, and Wyatt K. Metzger

JOURNAL OF APPLIED PHYSICS **120**, 105704 (2016)

Cathodoluminescence spectrum imaging analysis of CdTe thin-film bevels

John Moseley,[1,2,a)] Mowafak M. Al-Jassim,[1] Harvey L. Guthrey,[1] James M. Burst,[1] Joel N. Duenow,[1] Richard K. Ahrenkiel,[1,2] and Wyatt K. Metzger[1]
[1]*National Renewable Energy Laboratory, 15013 Denver West Parkway, Golden, Colorado 80401, USA*
[2]*Colorado School of Mines, 1500 Illinois Street, Golden, Colorado 80401, USA*

(Received 16 June 2016; accepted 24 August 2016; published online 9 September 2016)

We conducted $T = 6\,\mathrm{K}$ cathodoluminescence (CL) spectrum imaging with a nanoscale electron beam on beveled surfaces of CdTe thin films at the critical stages of standard CdTe solar cell fabrication. We find that the through-thickness CL total intensity profiles are consistent with a reduction in grain-boundary recombination due to the $CdCl_2$ treatment. The color-coded CL maps of the near-band-edge transitions indicate significant variations in the defect recombination activity at the micron and sub-micron scales within grains, from grain to grain, throughout the film depth, and between films with different processing histories. We estimated the grain-interior sulfur-alloying fraction in the interdiffused CdTe/CdS region of the $CdCl_2$-treated films from a sample of 35 grains and found that it is not strongly correlated with CL intensity. A kinetic rate-equation model was used to simulate grain-boundary (GB) and grain-interior CL spectra. Simulations indicate that the large reduction in the exciton band intensity and relatively small decrease in the lower-energy band intensity at CdTe GBs or dislocations can be explained by an enhanced electron-hole non-radiative recombination rate at the deep GB or dislocation defects. Simulations also show that higher GB concentrations of donors and/or acceptors can increase the lower-energy band intensity, while slightly decreasing the exciton band intensity. *Published by AIP Publishing.*
[http://dx.doi.org/10.1063/1.4962286]

I. INTRODUCTION

CdTe thin-film solar cell efficiencies are now competing directly with multicrystalline silicon (mc-Si) efficiencies at both the cell and module levels.[1,2] Further improvements can help CdTe solar technology to reach a levelized cost of electricity that is less than the conventional energy sources.[3] Yet, our inability to characterize and quantify the complex non-uniformities in composition, recombination, and defect chemistry in these microcrystalline layers continues to slow progress and encourage empiricism in the place of detailed understanding. Here, we report on high-resolution cathodoluminescence (CL) spectrum imaging with a nanoscale electron beam on beveled surfaces of CdTe thin films at the different stages of CdTe device fabrication to examine how the material properties fluctuate and can be characterized with this technique.

The interpretation of CL spectrum imaging data and the potential for this technique as a root-cause diagnostic tool for CdTe solar cells are underexplored. CL spectrum imaging combines the CL imaging and spectroscopy modes to provide a luminescence spectrum at each pixel in a scanning electron microscope (SEM) image.[4–6] Recently, this technique was applied on the back surfaces of CdTe thin films before and after the $CdCl_2$ treatment[7–9] and on a CdTe device cross-section.[10] In this work, we conduct CL spectrum imaging on *beveled surfaces* of CdTe films, which allows for a more in-depth examination of the small grains near the interdiffused CdTe/CdS interface than was achieved in the cross-sectional study.[10] A bevel etching technique, producing $<1°$ bevels with a large surface area, has previously allowed depth-dependent photoluminescence (PL) measurements on CdTe/CdS solar cells.[11] Here, we use a focused ion beam (FIB) to mill 20° bevels, which have less surface area and are better suited for high-pixel-density CL maps. We compare results on CdTe films after deposition, the $CdCl_2$ treatment, and back-contact formation including Cu insertion. We analyze the through-thickness total CL intensity profiles for the films, which show differences that are probably due to the effects of non-radiative grain-boundary (GB) recombination, grain size, and GB passivation. The color-coded CL maps are used to identify and analyze non-uniformities in composition, recombination, and defect chemistry. Furthermore, a low-temperature luminescence model is developed to help interpret differences between GB and grain-interior (GI) spectra.

II. EXPERIMENTAL

We analyzed CdTe films after typical stages in the fabrication of standard CdTe devices—i.e., after CdTe deposition, $CdCl_2$ treatment, and back-contact formation, including Cu insertion.[12,13] The corresponding thin-film structures and the sample names are listed in Table I. The Cu treatment diffused Cu into the CdTe layer during deposition of the ZnTe:Cu back contact at an elevated temperature. The CdTe thickness ranged from 3 to 4.1 μm. The deposition methods, times, temperatures, and other processing details for the samples can be found in Refs. 14 and 15.

The bevel-CL configuration used in this study is shown schematically in Fig. 1. This configuration eliminates the

a)Author to whom correspondence should be addressed. Electronic mail: john.moseley@nrel.gov

TABLE I. Structures of the samples and their assigned names.

Thin-film stack structure	Sample name
Glass/fluorine-doped SnO_2(FTO)/SnO_2(TO)/CdS/CdTe	As-deposited
Glass/FTO/TO/CdS/CdTe + $CdCl_2$ treatment	$CdCl_2$-treated
Glass/FTO/TO/CdS/CdTe + $CdCl_2$ treatment/ZnTe:Cu(2%)/Ti (metallization)	($CdCl_2$ + Cu)-treated

severe electron-beam charging that we have observed with the cross-sectional configuration and effectively extends the cross-sectional area by a factor of $1/\sin 20^\circ \sim 3$. Bevels were milled through the CdTe layer with a Ga^+ focused ion beam (FIB) (xT Nova NanoLab 200 FIB/SEM made by FEI Company). Prior to milling, a ~1-μm-thick layer of Pt was deposited to even out the top surface roughness and to protect the final analysis area from stray ions. The samples were tilted to form a 20° angle between the ion beam and the film surfaces. A 30-kV ion beam carved out the initial bevel shape, and a 5-kV beam created the final beveled surface to reduce surface damage. We expect the primary effects of residual FIB surface damage on the CL measurements to be an increased non-radiative surface recombination and a decreased radiative efficiency.

CL spectrum imaging was performed in a JEOL 7600F Schottky Field-Emission SEM with a Horiba H-CLUE CL system. Samples were cryogenically cooled in the SEM on a Gatan CF302 continuous-flow liquid-helium cold stage to a nominal temperature of 6 K. The SEM beam conditions were 5-kV accelerating voltage and about 1-nA current. With this electron-beam voltage, 60% of the carriers were generated within a ~100-nm depth below the surface and within a ~100-nm lateral range. (These values were determined by Monte Carlo electron energy-loss simulations using the CASINO software.[16]) The H-CLUE CL system uses a parabolic light-collection mirror and an iHR320 spectrometer equipped with a Syncerity thermoelectrically cooled charge-coupled device (CCD) detector (1024 × 256 pixels). The spectrum acquisition time was 5 ms, and the spectral resolution (or bandpass of the spectrograph) was estimated to be 8.5 meV at photon energy of 1.5 eV (given the 1-mm entrance slit width, 318.719-mm focal length, and dispersion by a grating with 600 gr/mm). Spectra shown are uncorrected for the spectral response of the CL system.

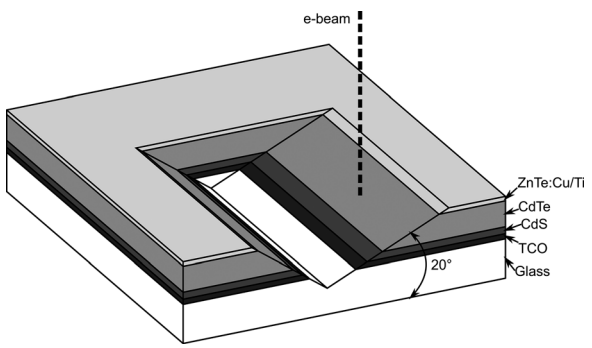

FIG. 1. An illustration of the bevel-CL configuration used in this study. The relative thicknesses of the layers are not to scale. The 20° bevels were prepared using a focused ion beam. Note that only the ($CdCl_2$ + Cu)-treated sample had the ZnTe:Cu/Ti top layer.

III. RESULTS AND DISCUSSION

Figure 2 shows the CL images (or maps) acquired on the beveled surfaces for the as-deposited, $CdCl_2$-treated, and ($CdCl_2$ + Cu)-treated samples along the top [(a) and (d)], middle [(b) and (e)], and bottom [(c) and (f)] rows, respectively. In the images, the back of the CdTe layer is at the top, and the CdTe/CdS interface is at the bottom. The white scale bar at the bottom right of each image is 0.5 μm, and the image widths are 20 to 25 μm. The left column [Figs. 2(a)–2(c)] shows the total CL intensity images integrated over the 1.386–1.610 eV near-band-edge spectral range at a low temperature (E_g = 1.606 eV at 5 K (Ref. 17)). After subtracting the background signal, the intensity in each image is normalized to the maximum intensity *in that image* (i.e., normalization is not universal across the images). In CL spectrum imaging, we collect a spectrum per pixel in an SEM image, which yields a 4-dimensional data space for each bevel area. The red-green-blue (RGB)-composite maps can be used to display the spectral features in two dimensions, as shown in the right column [Figs. 2(d)–2(f)]. To make the maps, the spectral range is first divided into three sub-ranges—1.386–1.500 eV, 1.500–1.575 eV, and 1.575–1.610 eV—that are assigned red, green, and blue colors, respectively. Each spectrum is normalized to the maximum intensity, and then, the total counts in each sub-range are normalized to the 0–255 red-green-blue color code. Sub-range energies were chosen to identify regions with primarily excitonic emission (blue), shallow defect emission (green), or donor-acceptor-pair (DAP) and electron-to-acceptor (eA^0) emission associated with deeper acceptors (red).

The intensities of the near-band-edge transitions in low-temperature luminescence spectra depend on the rates of competing charge-carrier capture and recombination processes occurring at defects.[18–20] The pixel color in Fig. 2 RGB-composite maps is impacted by the local concentrations of various shallow and deep defects, as well as a compositional change near the interdiffused CdTe/CdS interface due to bandgap bowing. A remarkable degree of color non-uniformity can be seen within grains, from grain to grain, through the thickness of films, and between samples with different processing histories. The features in the top half of the RGB-composite maps for the as-deposited and $CdCl_2$-treated samples [Figs. 2(d) and 2(e)] are very similar to the back-surface features that we have reported in Ref. 8. Briefly, the mostly blue color for the as-deposited sample indicates that the exciton recombination dominates within most of the GIs. Once $CdCl_2$ is introduced, the green color indicates relatively high concentrations of a shallow defect (with ~45-meV ionization energy[21]), which is believed to be a chlorine-cadmium vacancy (acceptor-like) complex.[21–23] Further details are discussed in Ref. 8. Here, we focus on: (1) changes in the CL total-intensity profiles resulting from the $CdCl_2$ and Cu treatments, (2) grain-to-grain spectral shifts near the interdiffused CdTe/CdS interface, and (3) GB vs. GI spectra, using the ($CdCl_2$ + Cu)-treated sample as an example.

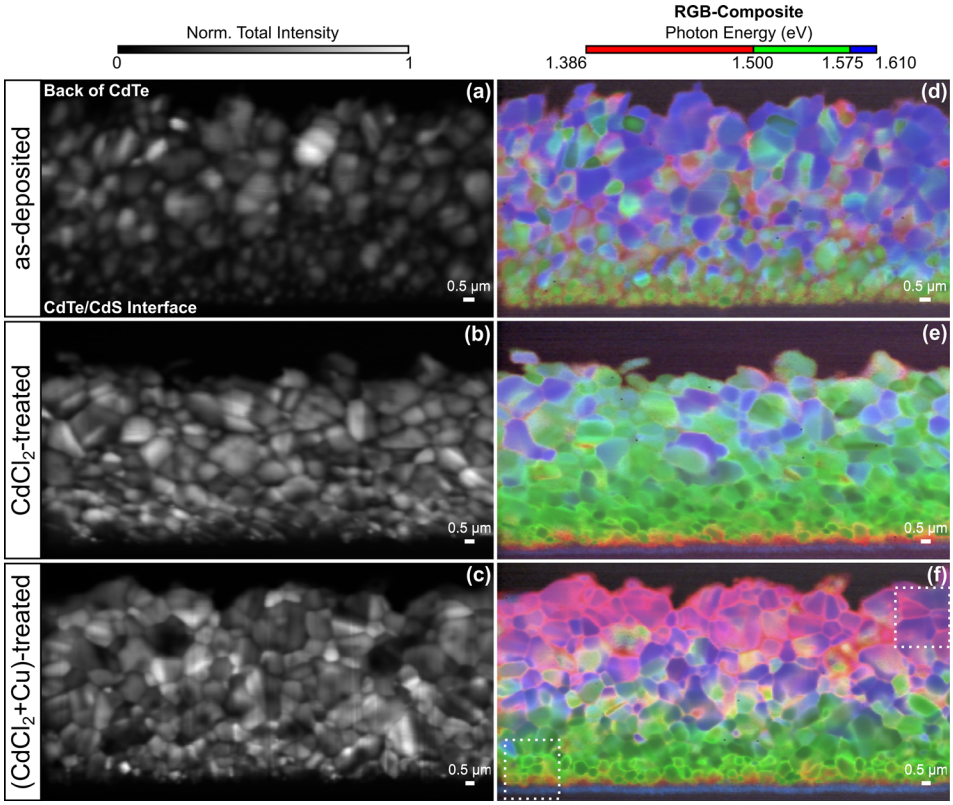

FIG. 2. The total CL intensity images in the left column [(a)–(c)] and the RGB-composite maps in the right column [(d)–(f)]. The top, middle, and bottom rows correspond to the as-deposited, $CdCl_2$-treated, and ($CdCl_2$ + Cu)-treated samples, respectively. The back of the CdTe layer is at the top, and the CdTe/CdS interface is at the bottom of each image. In the total CL intensity images, the intensity is normalized for each sample on a linear scale. The color bar above the RGB-composite maps indicates the dominant spectral range of the emission at each location.

A. Total CL intensity images and profiles

Figure 3 is a total CL intensity profile plot for the three samples, averaged over the entire image width in the left column of Fig. 2. The abscissa corresponds to the approximate distance *normal to the film thickness* (i.e., the up-down distance in the image multiplied by $\sin 20^\circ$), and the intensity is normalized for each sample. Prior to the $CdCl_2$ treatment, the intensity gradually increases from the CdTe/CdS interface into the CdTe layer for about 70% ($\sim$2.5 μm/3.5 μm) of the total layer thickness. After the $CdCl_2$ treatment, the intensity increases much more rapidly at the front of the CdTe and is more uniform through the CdTe layer.

The more gradual increase in CL intensity away from the CdTe/CdS interface for the as-deposited sample is probably due to the effects of non-radiative GB recombination, grain size, and GB passivation. GBs are darker than the GIs in the total CL intensity images [Figs. 2(a)–2(c)], especially for the as-deposited sample. This is most likely because dangling, distorted, or wrong bonds at GBs create high concentrations of deep levels that are non-radiative recombination centers.[24] For the as-deposited sample, the average grain size can be seen to increase gradually from about 0.5 μm in diameter near the CdTe/CdS interface to a couple of microns at the back of the CdTe. Thus, the as-deposited CL intensity profile exhibits an intensity increase with the increasing grain size and decreasing GB density, which we can expect for unpassivated GBs. The more square CL intensity profiles for the $CdCl_2$- and ($CdCl_2$ + Cu)-treated samples support the conclusion that the $CdCl_2$ treatment passivates a significant fraction of the GB deep levels.[25]

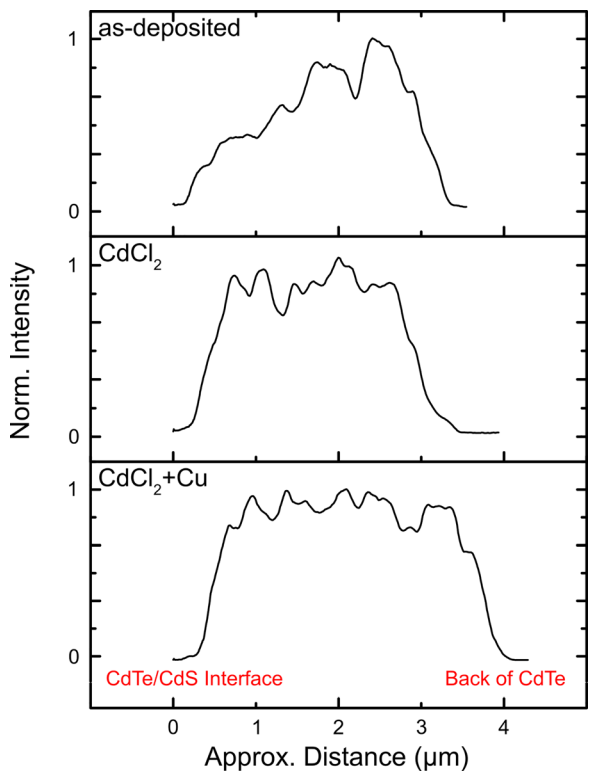

FIG. 3. The total CL intensity profiles plotted from the CdTe/CdS interface (located at about 0 μm) to the back of the CdTe for the as-deposited, $CdCl_2$-treated, and ($CdCl_2$ + Cu)-treated samples. These profiles are extracted from the grayscale CL images in Fig. 2.

B. RGB-composite maps

Here, we consider the RGB-composite maps in the right column of Fig. 2. One can see that the features near the CdTe/CdS interface are qualitatively similar for the $CdCl_2$- and ($CdCl_2$ + Cu)-treated samples [Figs. 2(e) and 2(f), respectively]. Perhaps the most striking features are the small green circles—each of which is a small grain. These grains have a darker-green GI color and a lighter-green GB color.

In Fig. 4, we show a zoomed-in image of the small area outlined with a dotted white line in the *bottom-left corner* of the ($CdCl_2$ + Cu) RGB-composite map [Fig. 2(f)]. The white scale bar in the zoomed-in image is 0.5 μm. Figure 4 plots the average spectrum for the dark-green pixels in the centers of two neighboring grains, labeled 1 and 2 in the image, and the spectrum at a light-green GB pixel between the grains (GB 1–2). (As a visual aid, the line color of each spectrum has been matched to its corresponding pixel color.) A single peak can be observed in the spectrum for each grain, whereas a double peak is observed in the GB spectrum. The GB peaks occur at about the same energies as those for the grains—1.534 eV for grain 1 and 1.556 eV for grain 2—but they have lower intensities. *Importantly, this is a general trend for the grains and GBs with a similar appearance (i.e., the "green grains") in the RGB-composite maps.* Also, for these grains, we observe a less peak-energy variation within a grain than from one grain to the next. This indicates that for carrier excitation in one of these GIs, a relatively small fraction of the total carriers diffuses and recombines radiatively in the neighboring grains; the majority of the CL signal is localized within the excited grain. We see signal from the adjoining grains only when exciting at a GB pixel, where the generation volume overlaps both the GIs.

It should be noted that the peak energies for grain 1 and grain 2 are considerably lower than those for excitonic transitions in "pure" CdTe at low temperature, which are located at 1.58–1.60 eV. It is well known that interdiffusion of CdTe and CdS can lead to CdS_xTe_{1-x} alloying. The bandgap of the resultant alloy, $E_g(CdS_xTe_{1-x})$, bows downward from the

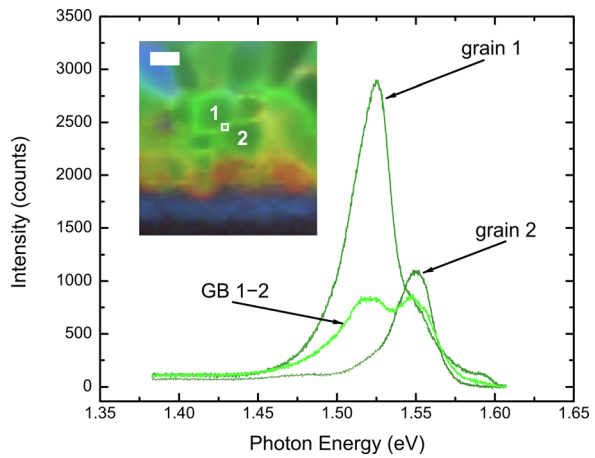

FIG. 4. Zoomed-in image of the small area delineated with a dotted white line in the *bottom-left corner* of the ($CdCl_2$ + Cu) RGB-composite map [Fig. 2(f)] and plots of the spectra within grains 1 and 2 and at the GB pixel between them (GB 1–2). The white scale bar in the image is 0.5 μm.

bandgaps of CdTe ($E_g(CdTe)$) and CdS ($E_g(CdS)$) according to the quadratic equation

$$E_g(CdS_xTe_{1-x}) = kx^2 + [E_g(CdS) - E_g(CdTe) - k]x + E_g(CdTe), \quad (1)$$

where k is the bowing parameter and x is the fraction of anion sites occupied by S.[11,26,27] In a low-temperature photoluminescence (PL) investigation of the CdTe/CdS interdiffusion and CdS_xTe_{1-x} alloying, Potter *et al.*[11] used Eq. (1) to estimate the x values from the PL peak energies. Their assumption was that the redshifts in peak energy relative to the CdTe exciton band peak energy were due entirely to the Te-rich CdS_xTe_{1-x} alloy formation. Using this approach, with the exciton band peak energy at the back of the CdTe in the ($CdCl_2$ + Cu)-sample as the low-temperature CdTe bandgap, $E_g(CdTe) \approx 1.591$ eV, and employing literature values of $k = 1.8$[28] and $E_g(CdS) = 2.50$ eV,[29] we estimate $x = 0.075$ for grain 1 and $x = 0.043$ for grain 2 in Fig. 4. This analysis suggests that the S concentration in *adjacent* grains in the interdiffused CdTe/CdS region can differ by a factor of 1.5–2.

The peak energy variation for the green grains can be seen in Fig. 5. Figure 5(a) shows the ($CdCl_2$ + Cu) RGB-composite map [Fig. 2(f)] near the CdTe/CdS interface, and Fig. 5(b) shows a grayscale map of the same area indicating the peak photon energy over the 1.500–1.560 eV range. Figure 5(c) plots the peak CL *intensity* vs. peak energy for *35* of the grains in Figs. 5(a) and 5(b). The peak energies are determined from the average spectrum in the GIs. The top axis corresponds to the estimated S alloying fraction (i.e., x in CdS_xTe_{1-x}) based on the peak energy. Aggregate studies have indicated that S diffusion during the $CdCl_2$ treatment can reduce recombination;[30–32] so, it is possible that the S diffusion fluctuations can be correlated with the lifetime and other material properties. However, this plot shows for the first time—for a fairly large sample of grains near the interdiffused CdTe/CdS interface—that there is no significant correlation between the GI CL intensity and the S alloying fraction. We estimate that $x = 0.080$ on average within the GIs, with a standard deviation of $x = 0.021$. The average value equates to an S concentration of 4.0 at. %, which agrees well with GI concentrations determined from the recent atom-probe tomography data for three grains near the CdTe/CdS interface (in a sample with similar processing to the one examined here): ~5, ~4, and ~3 at. %.[33]

The RGB-composite maps in Fig. 2 illustrate interesting trends near the back of the CdTe. Comparing the pixel color in the maps across the samples, there is a progressive redshift in the dominant spectral sub-range after the $CdCl_2$ and Cu treatments. In Ref. 8, we analyzed changes occurring in the RGB-composite maps in the back surface CL as a result of the $CdCl_2$ treatment. In this work, we analyze the bright-red lines near the back of the CdTe in the RGB-composite map for the ($CdCl_2$ + Cu)-treated sample, which are clearly GB signatures induced by the Cu treatment.

In Fig. 6, we show a zoomed-in image of the small area outlined with the dotted white line in the *top-right corner* of

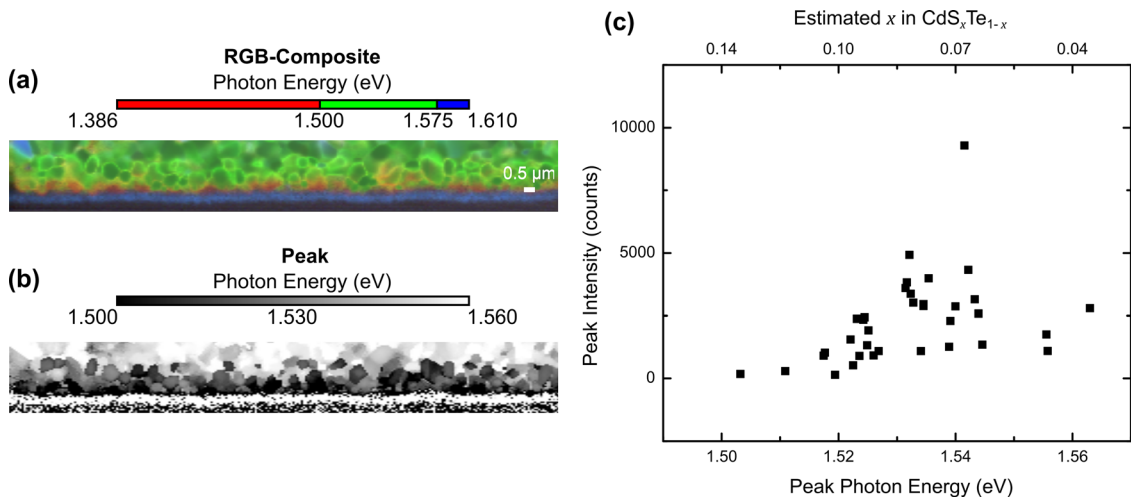

FIG. 5. (a) ($CdCl_2 + Cu$) RGB-composite map [Fig. 2(f)] near the CdTe/CdS interface and (b) grayscale map of the same area indicating the peak photon energy over the 1.500–1.560 eV range. (c) The peak CL *intensity* vs. peak energy for *35* of the grains in (a) and (b). The top axis corresponds to the estimated x in CdS_xTe_{1-x} using Eq. (1); note that the scale is only approximately linear over this compositional range.

the ($CdCl_2 + Cu$) RGB-composite map [Fig. 2(f)]. The GB and GI spectra for this area are also plotted in Fig. 6. The spectra are averages within the white boxes in the image, and the intensities have been normalized to the GI maximum. Two "bands" can be identified in the spectra: one in the 1.575–1.61 eV energy range and a relatively broad lower-energy band with a maximum at ~1.43 eV. The higher-energy band is due to exciton transitions, and the lower-energy band is believed to be due to donor-acceptor-pair (DAP) transitions and electron-to-acceptor (eA^0) transitions involving Cu_{Cd} acceptors with a defect activation energy of about 100–120 meV.[34,35] Note that the DAP and eA^0 transitions and their associated phonon replica are overlapping and not resolvable in Fig. 6.

In the Fig. 6 spectra, the exciton band intensity is significantly reduced at the GB relative to the GI (GB intensity/GI intensity is about 0.50 at peak), whereas the lower-energy band intensity increases to some extent. For the GIs and GBs in Fig. 2(f) with a similar appearance to those in Fig. 6, we have found that the exciton band intensity is always significantly reduced at the GB relative to the GI. The lower-energy band intensity may increase at the GB, as in Fig. 6, or decrease, but the relative decrease is generally less than that for the exciton band. Other authors have remarked on similar trends occurring at the GBs in the CdTe thin films[36] and dislocations in epitaxially grown single-crystal CdTe films[37] in CL or micro-photoluminescence studies conducted at liquid-nitrogen temperature. It has been proposed that exciton recombination becomes non-radiative at the GBs or dislocations. However, exciton non-radiative recombination seems improbable given that the excitons recombine with energy almost equal to the bandgap. In Section III C, we describe a low-temperature luminescence model that provides an alternative explanation for the significant decrease in the exciton band intensity at GBs and dislocations in CdTe and accounts for the less significant intensity decrease for the lower-energy band. Simulated spectra also confirm the more obvious conclusion that, when the intensity of the lower-energy band is increased at a GB, as in Fig. 6, higher GB concentrations of (radiative) donor and/or acceptor defects are likely.

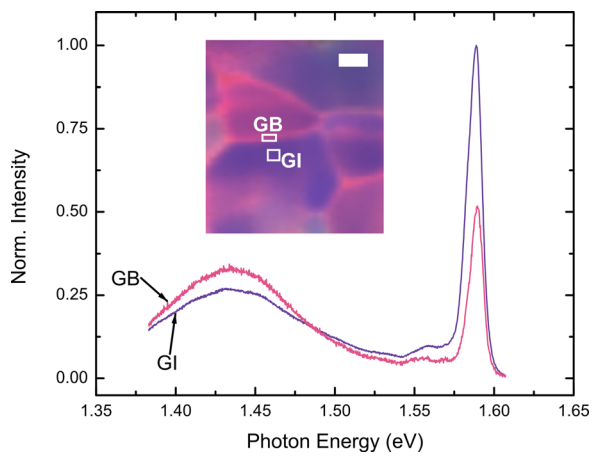

FIG. 6. Zoomed-in image of the small area delineated with the dotted white line in the *top-right corner* of the ($CdCl_2 + Cu$) RGB-composite map [Fig. 2(f)] and plots of the GB and GI CL spectra normalized to the maximum GI intensity. The (solid) white scale bar in the image is 0.5 μm.

C. Low-temperature luminescence model and spectrum simulations

The low-temperature luminescence model described here is based on the rate-equation models developed by Schmidt *et al.*[18] and Reshchikov *et al.*[19,20] As depicted in Fig. 7 energy-band schematic, a number of carrier capture and recombination processes are possible during a low-temperature luminescence experiment. The rate of each process can be determined by solving a system of kinetic rate equations, which accounts for all of the processes occurring in parallel.

Radiative and non-radiative processes are considered at three types of defects: shallow donor, shallow acceptor, and (donor-like) deep defects. The recombination events occurring at the shallow donors and acceptors are assumed to be only radiative, and recombination at deep defects is taken to be only non-radiative. Prior to recombination events, carriers—electrons, holes, and excitons—must become trapped or bound at the defects (except in the case of free-exciton

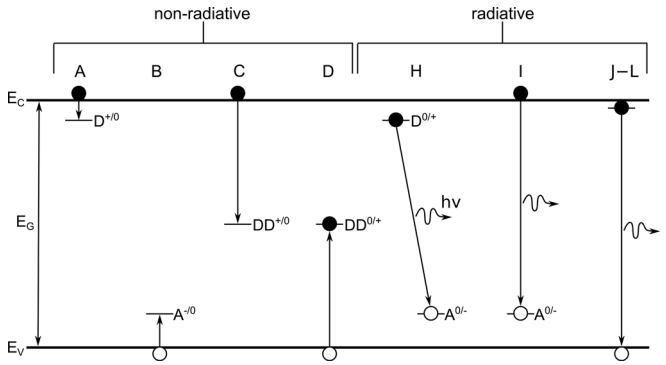

FIG. 7. A schematic band diagram of the non-radiative and radiative processes in the low-temperature luminescence model described in the text. E_C, E_V, and E_G are the conduction, valence, and bandgap energies, respectively. Processes E–G are not shown in the diagram.

recombination). Trapping is a non-radiative carrier capture process, which, in terms of Fig. 7 band diagram, involves the transition by a carrier from the conduction or valence band to a defect level.

The non-radiative processes are illustrated on the left side of Fig. 7. In process A, an ionized donor (D^+) captures a free electron in the conduction band to form a neutral donor (D^0). Likewise, in process B, an ionized acceptor (A^-) captures a free hole in the valence band to form a neutral acceptor (A^0). A positively charged deep defect (DD^+) can also capture a free electron to form a neutral level (DD^0) in process C. In process D, a neutral deep defect captures a free hole, resulting in non-radiative recombination (and restoring the positive charge on the deep defect). We assume that excess carriers are initially generated as electrons and holes, which can thereafter bind to form free excitons in process E. A donor or acceptor bound exciton is formed when a free exciton is captured by a neutral donor or neutral acceptor in processes F and G, respectively. Non-radiative processes E–G are not shown in Fig. 7. As in the model by Schmidt *et al.*,[18] we neglect the inverse capture processes (i.e., thermal reemission) as well as the free-exciton dissociation.

Possible radiative transitions are shown on the right side of Fig. 7. Process H involves transitions between acceptor-bound holes and donor-bound electrons (or DAP transitions); process I involves transitions between free electrons and acceptor-bound holes (or eA^0 transitions); and processes J–L involve free- and bound-exciton transitions. Note that transitions involving the bound carriers return the defects to their unbound state. For example, a DAP transition leaves both the donor and acceptor in the ionized state (i.e., D^+ and A^-) such that the defects can capture the carriers again.

The rate of each process is taken to be proportional to the concentrations of the carriers and/or defects involved and a characteristic rate constant or a lifetime in the case of exciton radiative recombination.[18–20] For example, the rate of radiative eA^0 transitions is $C_{nA}N_A^0 n$—where C_{nA} is the eA^0 transition rate constant (process I). Thus, the rates of processes A–L are described by the following system of equations:

$$\frac{\partial n}{\partial t} = G - C_X np - C_{nD}N_D^+ n - C_{nA}N_A^0 n - C_{nDD}N_{DD}^+ n = 0, \tag{2}$$

$$\frac{\partial p}{\partial t} = G - C_X np - C_{pA}N_A^- p - C_{pDD}N_{DD}^0 p = 0, \tag{3}$$

$$\frac{\partial n_X}{\partial t} = C_X np - \frac{n_X}{\tau_X} - C_{DX}N_D^0 n_X - C_{AX}N_A^0 n_X = 0, \tag{4}$$

$$\frac{\partial N_{DX}}{\partial t} = C_{DX}N_D^0 n_X - \frac{N_{DX}}{\tau_{DX}} = 0, \tag{5}$$

$$\frac{\partial N_{AX}}{\partial t} = C_{AX}N_A^0 n_X - \frac{N_{AX}}{\tau_{AX}} = 0, \tag{6}$$

$$\frac{\partial N_{DD}^0}{\partial t} = C_{nDD}N_{DD}^+ n - C_{pDD}N_{DD}^0 p = 0, \tag{7}$$

$$\frac{\partial N_D^0}{\partial t} = C_{nD}N_D^+ n + \frac{N_{DX}}{\tau_{DX}} - C_{DX}N_D^0 n_X - C_{DA}N_D^0 N_A^0 = 0, \tag{8}$$

$$\frac{\partial N_A^0}{\partial t} = C_{pA}N_A^- p + \frac{N_{AX}}{\tau_{AX}} - C_{AX}N_A^0 n_X - C_{nA}N_A^0 n - C_{DA}N_D^0 N_A^0 = 0, \tag{9}$$

$$p + N_D^+ + N_{DD}^+ = n + N_A^-. \tag{10}$$

Listed in respective order: G is the electron-beam generation rate of electrons and holes [$cm^{-3}s^{-1}$]; n, p, and n_X are the free electron, hole, and exciton concentrations [cm^{-3}], respectively; $N_D^+(N_D^0)$, $N_A^-(N_A^0)$, and $N_{DD}^+(N_{DD}^0)$ are the ionized (neutral) donor, acceptor, and deep defect concentrations, respectively; N_{DX} and N_{AX} are the donor- and acceptor-bound exciton concentrations, respectively; the rate constants for processes A–I are C_{nD}, C_{pA}, C_{nDD}, C_{pDD}, C_X, C_{DX}, C_{AX}, C_{DA}, and C_{nA} [$cm^3\ s^{-1}$], respectively; and the lifetimes for processes J–L are τ_X, τ_{DX}, and τ_{AX} [s^{-1}], respectively. Equations (2)–(9) reflect the fact that, in steady state, there is no change in the carrier or defect concentrations. The last equation (Eq. (10)) ensures that the system is charge neutral.

Using reasonable values for the rate constants and lifetimes, we numerically solve Eqs. (2)–(10) to obtain the radiative transition rates.[20] The only independent variables are N_D, N_A, and N_{DD}, which are the *total* concentrations of donors, acceptors, and deep defects, respectively (e.g., $N_D = N_D^+ + N_D^0$). As a check on the solutions of Eqs. (2)–(10), we verify that the total recombination rate equals the total generation rate (steady state). The spectra can be simulated if the luminescence lineshapes are known. We assume that the analytical form of the lineshapes is given by the product of a Poisson distribution and a Gaussian function (see, for example, Ref. 38, Eq. (A4)).

Figure 8 shows the simulated GI and GB spectra, normalized to the GI maximum intensity. For the GI spectrum, values of $N_D = 2 \times 10^{16}$, $N_A = 7 \times 10^{16}$, and $N_{DD} = 1 \times 10^{18}$ cm^{-3} were chosen to match the qualitative characteristics of the experimental GI spectrum in Fig. 6. (Note that the generation volume size, carrier diffusion, and surface recombination are not explicitly accounted for in the model; so, these concentrations are necessarily "effective" values.) To simulate

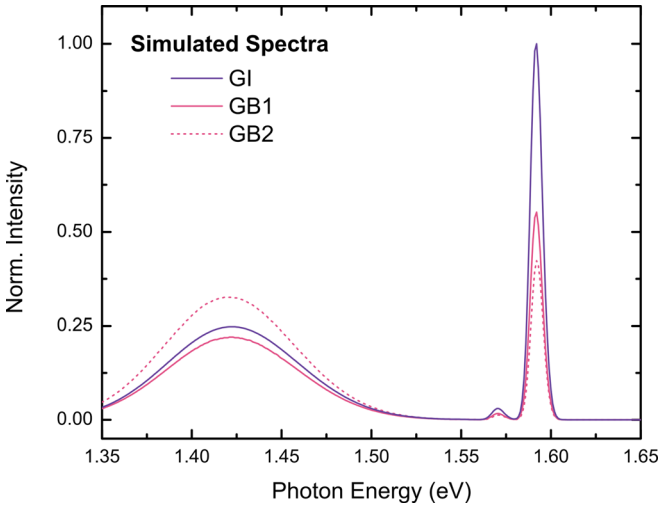

FIG. 8. Simulated GI and GB spectra based on the low-temperature luminescence model discussed in the text. For the GI spectrum, $N_D = 2\times10^{16}$, $N_A = 7\times10^{16}$, and $N_{DD} = 1\times10^{18}\,\mathrm{cm}^{-3}$. For GB spectrum 1 (GB1), $N_D = 2\times10^{16}$, $N_A = 7\times10^{16}$, and $N_{DD} = 1.5\times10^{18}\ \mathrm{cm}^{-3}$. For GB spectrum 2 (GB2), $N_D = 4\times10^{16}$, $N_A = 7\times10^{16}$, and $N_{DD} = 1.5\times10^{18}\,\mathrm{cm}^{-3}$. The rate constants and lifetimes used in the simulations are: $G = 10^{26}\ \mathrm{cm}^{-3}\mathrm{s}^{-1}$, $C_{nD} = C_{pA} = C_X = 10^{-8}\,\mathrm{cm}^3\mathrm{s}^{-1}$, $C_{nDD} = C_{pDD} = 10^{-6}\,\mathrm{cm}^3\mathrm{s}^{-1}$, $C_{DX} = C_{AX} = 10^{-7}\,\mathrm{cm}^3\mathrm{s}^{-1}$, $C_{nA} = C_{DA} = 10^{-11}\ \mathrm{cm}^3\,\mathrm{s}^{-1}$, and $0.1\tau_X = \tau_{DX} = \tau_{AX} = 10^{-10}\ \mathrm{s}^{-1}$.

the GB spectra, we coarsely adjust N_D, N_A, and N_{DD} from the GI values, holding the other parameters (rate constants, lifetimes, and lineshape) constant (see Fig. 8 caption). While the simulation results are sensitive to the choice of parameter values, we find that the *trends* discussed below are valid over a broad range of values.

In GB spectrum 1 (GB1), the concentration of deep defects is increased to $N_{DD} = 1.5\times10^{18}\ \mathrm{cm}^{-3}$, or 1.5× the GI value, which gives a GB exciton band peak intensity that is about half the GI intensity, as observed in Fig. 6 experimental spectra. The non-radiative recombination rate at deep defects is proportional to N_{DD}^0. Thus, according to the simulations, the significant reduction in the exciton band intensity observed at GBs and dislocations can be explained by enhanced electron-hole non-radiative recombination at deep defects, which have higher concentrations at GBs and dislocations. In other words, the model can describe the decrease in the exciton band intensity observed in Fig. 6 and in other studies[36,37]—without having to invoke the existence of a non-radiative exciton recombination. Consistent with the experimental spectra, GB spectrum 1 shows that deep-defect recombination has a greater relative impact on the intensity of the exciton transitions than the lower-energy transitions.

In GB spectrum 2 (GB2), $N_{DD} = 1.5\times10^{18}\ \mathrm{cm}^{-3}$ (as with GB1), and the donor concentration is increased 2× above the GI value to (roughly) match the intensity of the lower-energy transitions in Fig. 6 GB spectrum; alternatively, the acceptor concentration can be increased to achieve about the same result due to the overlap between the DAP and eA^0 transitions and their associated phonon replica. However, an increased concentration of GB donors is consistent with GB depletion, which has been determined by scanning-probe microscopy measurements on CdTe thin films at different stages in solar cell processing.[39–41] Interestingly, increasing the donor concentration has also caused a slight decrease in the exciton band intensity (compare GB1 and GB2), which is an unexpected consequence of the competing luminescence processes. As discussed earlier, for the GIs and GBs in Fig. 2(f) with a similar appearance to those in the Fig. 6, the lower-energy band intensity may increase at the GB, as in Fig. 6, or decrease. The results in Fig. 8 confirm the more obvious conclusion that, when the intensity of the lower-energy band is increased at a GB, higher GB concentrations of (radiative) donor and/or acceptor defects are likely.

IV. SUMMARY

We presented the high-resolution cathodoluminescence (CL) spectrum imaging results on beveled surfaces of CdTe thin films at the critical stages of standard solar cell device fabrication. We found that the through-thickness total CL intensity profiles are consistent with a reduction in grain-boundary (GB) recombination due to the $CdCl_2$ treatment. The color-coded CL maps revealed variations in the recombination activity of defects on the micron and sub-micron scales. Significant variations are apparent in the maps within grains, from grain to grain, through the thickness of films, and between films with different processing histories. The grain-to-grain sulfur-alloying fraction in the interdiffused CdTe/CdS region of a $CdCl_2$-treated film was estimated from a sample of 35 grains. Although previous studies indicate that S diffusion during the $CdCl_2$ treatment reduces recombination, our results suggest that the grain-interior CL intensity is uncorrelated with the sulfur-alloying fraction.

We described a low-temperature luminescence model in which rate equations are used to account for competing carrier capture and recombination processes. Simulations of spectra indicate that the large reduction in the exciton band intensity and relatively small decrease in the lower-energy band intensity at CdTe GBs or dislocations can be explained by an enhanced electron-hole non-radiative recombination rate at deep GB or dislocation defects. Simulations also show that higher GB concentrations of donors and/or acceptors can increase the lower-energy band intensity, while slightly decreasing the exciton band intensity.

The data presented here indicate that combining high-resolution cathodoluminescence spectrum imaging on beveled surfaces with rate-equation modeling can enhance the ability to characterize and quantify the complex non-uniformities in composition, recombination, and defect chemistry in microcrystalline layers for opto-electronic applications.

ACKNOWLEDGMENTS

This research was supported by the U.S. Department of Energy, Office of Energy Efficiency and Renewable Energy, under Contract No. DE-AC36-08GO28308.

[1]M. A. Green, K. Emery, Y. Hishikawa, W. Warta, and E. D. Dunlop, Prog. Photovoltaics **24**(1), 3–11 (2016).
[2]M. A. Green, Nat. Energy **1**, 15015 (2016).
[3]See http://www.energy.gov/sites/prod/files/2015/09/f26/NREL%20Paper%2009-16-15.pdf for "Technology Advances Needed for Photovoltaics to Achieve Widespread Grid Price Parity" (accessed June 1, 2016).

[4]C. M. Parish and P. E. Russell, "Scanning cathodoluminescence microscopy," Adv. Imaging Electron Phys. **147**, 1–135 (2007).
[5]D. Abou-Ras, M. Nichterwitz, M. J. Romero, and S. S. Schmidt, "Electron microscopy on thin films for solar cells," in *Advanced Characterization Techniques for Thin Film Solar Cells*, edited by U. Rau, D. Abou-Ras, and T. Kirchartz (John Wiley & Sons, 2011).
[6]P. R. Edwards and R. W. Martin, Semicond. Sci. Technol. **26**(6), 064005 (2011).
[7]J. Moseley, M. Al-Jassim, H. Moutinho, H. Guthrey, W. Metzger, and R. Ahrenkiel, Appl. Phys. Lett. **103**(23), 233103 (2013).
[8]J. Moseley, M. M. Al-Jassim, D. Kuciauskas, H. R. Moutinho, N. Paudel, H. L. Guthrey, Y. Yan, W. K. Metzger, and R. K. Ahrenkiel, IEEE J. Photovoltaics **4**(6), 1671–1679 (2014).
[9]B. Mendis, D. Gachet, J. Major, and K. Durose, Phys. Rev. Lett. **115**(21), 218701 (2015).
[10]A. Taylor, J. Major, G. Kartopu, D. Lamb, J. Duenow, R. Dhere, X. Maeder, S. Irvine, K. Durose, and B. Mendis, Sol. Energy Mater. Sol. Cells **141**, 341–349 (2015).
[11]M. Potter, D. Halliday, M. Cousins, and K. Durose, Thin Solid Films **361**, 248–252 (2000).
[12]J. D. Poplawsky, N. R. Paudel, C. Li, C. M. Parish, D. Leonard, Y. Yan, and S. J. Pennycook, Adv. Energy Mater. **4**(15), 1400454 (2014).
[13]B. A. Korevaar, G. Zorn, K. C. Raghavan, J. R. Cournoyer, and K. Dovidenko, Prog. Photovoltaics **23**(11), 1466–1474 (2015).
[14]J. Burst, W. Rance, T. Barnes, M. Reese, J. Li, D. Kuciauskas, M. Steiner, T. Gessert, K. Zhang, and C. Hamilton, paper presented at the 2012 38th IEEE Photovoltaic Specialists Conference (PVSC), 2012.
[15]W. Rance, J. M. Burst, M. O. Reese, D. Meysing, C. A. Wolden, T. A. Gessert, S. Garner, P. Cimo, and T. M. Barnes, paper presented at the 2013 IEEE 39th Photovoltaic Specialists Conference (PVSC), 2013.
[16]H. Demers, N. Poirier-Demers, M. R. Phillips, N. de Jonge, and D. Drouin, Microsc. Microanal. **18**(06), 1220–1228 (2012).
[17]C. Kraft, H. Metzner, M. Hädrich, U. Reislöhner, P. Schley, G. Gobsch, and R. Goldhahn, J. Appl. Phys. **108**(12), 124503 (2010).
[18]T. Schmidt, K. Lischka, and W. Zulehner, Phys. Rev. B **45**(16), 8989 (1992).
[19]M. A. Reshchikov, A. A. Kvasov, M. F. Bishop, T. McMullen, A. Usikov, V. Soukhoveev, and V. A. Dmitriev, Phys. Rev. B **84**(7), 075212 (2011).
[20]M. A. Reshchikov, J. Appl. Phys. **115**(1), 012010 (2014).
[21]H.-Y. Shin and C.-Y. Sun, J. Cryst. Growth **186**(3), 354–361 (1998).
[22]V. Consonni, G. Feuillet, J. Bleuse, and F. Donatini, J. Appl. Phys. **101**(6), 063522 (2007).
[23]V. Consonni, G. Feuillet, and S. Renet, J. Appl. Phys. **99**(5), 053502 (2006).
[24]D. B. Holt and B. G. Yacobi, *Extended Defects in Semiconductors: Electronic Properties, Device Effects and Structures* (Cambridge University Press, 2007).
[25]J. Moseley, W. K. Metzger, H. R. Moutinho, N. Paudel, H. L. Guthrey, Y. Yan, R. K. Ahrenkiel, and M. M. Al-Jassim, J. Appl. Phys. **118**(2), 025702 (2015).
[26]K. Ohata, J. Saraie, and T. Tanaka, Jpn. J. Appl. Phys., Part 1 **12**(8), 1198 (1973).
[27]R. Pal, J. Dutta, S. Chaudhuri, and A. Pal, J. Phys. D: Appl. Phys. **26**(4), 704 (1993).
[28]B. E. McCandless and J. R. Sites, "Cadmium telluride solar cells," in *Handbook of Photovoltaic Science and Engineering*, edited by A. Luque and S. Hegedus, 2nd ed. (John Wiley & Sons, 2011).
[29]*Semiconductors: Basic Data*, 2nd ed., edited by O. Madelung (Springer, Berlin, 1982).
[30]W. Metzger, D. Albin, D. Levi, P. Sheldon, X. Li, B. Keyes, and R. Ahrenkiel, J. Appl. Phys. **94**(5), 3549–3555 (2003).
[31]W. Metzger, D. Albin, M. Romero, P. Dippo, and M. Young, J. Appl. Phys. **99**(10), 103703 (2006).
[32]L. Kranz, C. Gretener, J. Perrenoud, D. Jaeger, S. S. Gerstl, R. Schmitt, S. Buecheler, and A. N. Tiwari, Adv. Energy Mater. **4**(7), 1301400 (2014).
[33]J. D. Poplawsky, C. Li, N. R. Paudel, W. Guo, Y. Yan, and S. J. Pennycook, Sol. Energy Mater. Sol. Cells **150**, 95–101 (2016).
[34]D. Kuciauskas, P. Dippo, Z. Zhao, L. Cheng, A. Kanevce, W. K. Metzger, and M. Gloeckler, IEEE J. Photovoltaics **5**(1), 366–371 (2015).
[35]W. Stadler, D. Hofmann, H. Alt, T. Muschik, B. Meyer, E. Weigel, G. Müller-Vogt, M. Salk, E. Rupp, and K. Benz, Phys. Rev. B **51**(16), 10619 (1995).
[36]M. J. Romero, D. S. Albin, M. M. Al-Jassim, X. Wu, H. R. Moutinho, and R. G. Dhere, Appl. Phys. Lett. **81**(16), 2962–2964 (2002).
[37]K. Alberi, B. Fluegel, M. J. DiNezza, S. Liu, Y.-H. Zhang, and A. Mascarenhas, Appl. Phys. Express **7**(6), 065503 (2014).
[38]A. Alkauskas, M. D. McCluskey, and C. G. Van de Walle, J. Appl. Phys. **119**(18), 181101 (2016).
[39]I. Visoly-Fisher, S. R. Cohen, K. Gartsman, A. Ruzin, and D. Cahen, Adv. Funct. Mater. **16**(5), 649–660 (2006).
[40]C.-S. Jiang, H. R. Moutinho, R. Dhere, and M. Al-Jassim, IEEE J. Photovoltaics **3**(4), 1383–1388 (2013).
[41]M. Tuteja, P. Koirala, V. Palekis, S. MacLaren, C. S. Ferekides, R. W. Collins, and A. A. Rockett, J. Phys. Chem. C **120**(13), 7020–7024 (2016).